JACS
JOURNAL OF THE AMERICAN CHEMICAL SOCIETY

Article

pubs.acs.org/JACS

Hydrophobic Molecules Infiltrating into the Poly(ethylene glycol) Domain of the Core/Shell Interface of a Polymeric Micelle: Evidence Obtained with Anomalous Small-Angle X-ray Scattering

Yusuke Sanada,[†] Isamu Akiba,[†] Kazuo Sakurai,*[,†] Kouichi Shiraishi,[‡] Masayuki Yokoyama,[‡] Efstratios Mylonas,[§] Noboru Ohta,[§] Naoto Yagi,[§] Yuya Shinohara,[∥] and Yoshiyuki Amemiya[∥]

[†]Department of Chemistry and Biochemistry, The University of Kitakyushu, 1-1 Hibikino, Wakamatsu-ku, Kitakyushu, Fukuoka 808-0135, Japan

[‡]Medical Engineering Laboratory, Research Center for Medical Science, The Jikei University School of Medicine, 3-25-8 Nishi-shinbashi, Minato-ku, Tokyo 105-8461, Japan

[§]Japan Synchrotron Radiation Research Institute (JASRI/SPring-8), 1-1-1 Kouto, Sayo, Sayo, Hyogo 679-5198, Japan

[∥]Department of Advanced Materials Science, Graduate School of Frontier Sciences, The University of Tokyo, 5-1-5 Kashiwanoha, Kashiwa, Chiba 277-8561, Japan

Supporting Information

ABSTRACT: Polymeric micelles have been extensively studied as nanoscale drug carriers. Knowing the inner structure of polymeric micelles that encapsulate hydrophobic drugs is important to design effective carriers. In our study, the hydrophobic compound tetrabromocathecol (TBC) was chosen as a drug-equivalent model molecule. The bromine atoms in TBC act as probes in anomalous small-angle X-ray scattering (ASAXS) allowing for its localization in the polymeric micelles whose shape and size were determined by normal small-angle X-ray scattering (SAXS). Light scattering measurements coupled with field flow fractionation were also carried out to determine the aggregation number of micelles. A core−corona spherical model was used to explain the shape of the micelles, while the distribution of bromine atoms was explained with a hard-sphere model. Interestingly, the radius of the spherical region populated with bromine atoms was larger than the one of the sphere corresponding to the hydrophobic core of the micelle. This result suggests that the TBC molecules infiltrate the PEG hydrophilic domain in the vicinity of the core/shell interface. The results of light scattering and SAXS indicate that the PEG chains at the shell region are densely packed, and thus the PEG domain close to the interface has enough hydrophobicity to tolerate the presence of hydrophobic compounds.

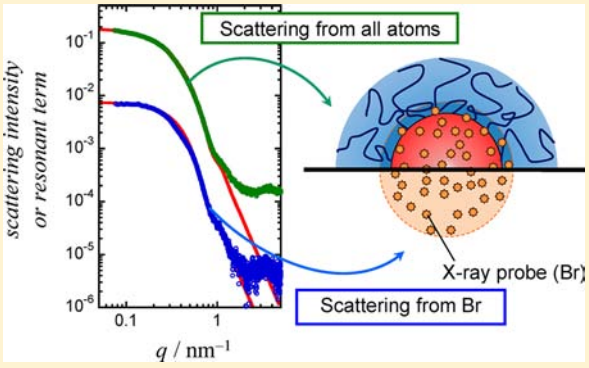

INTRODUCTION

Amphipathic block copolymers in aqueous solutions undergo microphase separation into hydrophobic and hydrophilic domains. When the polymer concentration is low enough, stable micelles are formed. By changing the chain-length ratio between the two blocks, the morphology of polymeric micelles can be controlled to spheres, plates, cylinders, or other complicated shapes.[1,2] In the case of long hydrophilic blocks, stable spherical micelles consisting of a hydrophobic core and a hydrophilic shell are obtained. The aggregation number of the spherical micelles is determined by both the hydrophobicity and the chain length of the core.[2] The chemical structure and the length of the hydrophilic block play an important role in determining the solubility of the micelles and in protecting them from secondary aggregation.[3]

Polymeric micelles have great potential as a drug delivery system (DDS), because the core can encapsulate hydrophobic drugs and the shell can provide biocompatibility, that is, preventing the micelles from blood clearance and protecting the drugs against unfavorable interactions such as adsorption on serum proteins. In recent decades, several kinds of block copolymers were studied for their application as DDS.[4−6] The combination of poly(ethylene glycol) (PEG) with an aspartic acid derivative is suitable for DDS, because of low toxicity, biodegradability, and excellent biocompatibility. PEG protects the micelle from unspecific protein binding, a process known as the "stealth effect".[7] The aspartic block is easily synthesized from a ring-opening reaction[8] and chemically modified with a variety of postpolymerization techniques.[9]

Kataoka et al.[10,11] used adriamycin-conjugated poly(ethylene glycol)-*block*-poly(aspartic acid), in which the anticancer drug

Received: September 9, 2012
Published: January 31, 2013

was buried in the hydrophobic core, conjugated with the poly(aspartic acid) block. Adams et al.[12] synthesized poly(ethylene oxide)-*block*-poly(6-hydroxylhexyl-L-aspartamide), which can encapsulate the antifungal drug amphotericin B, and studied the encapsulating and releasing behavior. Among others, poly(ethylene glycol)-*block*-poly(partially benzyl-esterified aspartic acid), denoted by PEG-P[Asp(Bzl)] (chemical structure shown in Scheme 1), is one of the most extensively

Scheme 1. Chemical Structures of PEG-P[Asp(Bzl)] and TBC[a]

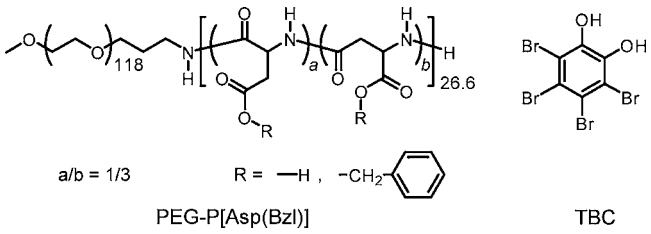

[a]The benzyl esterification and the α or β amid-linkage of the aspartic acid randomly occurred.[13]

studied systems in terms of therapeutic application.[13] These pioneering studies, while providing improvements in respect to practical applications, were mostly phenomenalistic, and the detailed architecture and structure of these micelles containing drugs is not clear.

Small-angle scattering with neutron and synchrotron X-ray (SAXS) sources has been instrumental in the clarification of the inner structures of polymeric micelles.[2] Our group carried out a SAXS study of a series of PEG-P[Asp(Bzl)] samples with different Asp/Bzl compositions and Asp length. The major factor determining the aggregation number was the benzylation ratio of the Asp chain (i.e., hydrophobicity of the chain), and the overcrowding of the tethered PEG chains increased about 2−3 times with increasing aggregation number, as compared to the unperturbed state.[14] Knowing how the drugs are distributed inside the core helps us understand the drug-releasing mechanism and increase the drug loading ratio. However, such information is difficult to obtain because the core size is normally less than 100 nm and the drug concentration is normally less than about 10 wt %, which makes it difficult to observe with electron microscopic techniques.

The third generation of synchrotron beamlines[15] made possible the execution of anomalous small-angle X-ray scattering (ASAXS) experiments on soft materials, because they can provide very bright and stable X-rays with variable wavelength at extreme accuracy. Anomalous scattering techniques were originally developed in the fields of inorganic and solid chemistry, such as catalysts, etc.,[16] but the same principles can be applied to the study of solutions of soft materials. Stuhrmann et al.[17] used ASAXS to observe the conformation of a polyelectrolyte brush, and Dingenouts et al.[18] studied the dispersion of counterions surrounding a polyelectrolyte. In these studies, the scattering information of the probe atom, called resonant term, was analytically obtained from the measurements. The resonant term essentially contains information only about the spatial distribution of the probe atoms. In this work, we chose PEG-P[Asp(Bzl)] as a block copolymer forming polymeric micelles and tetrabromocathecol (TBC, shown in Scheme 1) as an X-ray probe, and we tried to clarify how TBC is distributed inside the micelle core, using ASAXS.

EXPERIMENTAL SECTION

Materials, Sample Preparation, and Characterization. The block copolymer PEG-P[Asp(Bzl)] used in this study was prepared in the manner shown in our previous article.[13] By use of ^{1}H NMR, the average number of aspartic units and its benzyl esterified molar ratio were determined to be 26.9 and 83.3 mol %, respectively. We denote this sample A27-B83 hereinafter. The critical micellar concentration (CMC) of A27-B83 was determined by means of a hydrophobic fluorescence probe pyrene, which has been used for other polymeric micelles.[19] The obtained CMC was 2.2×10^{-3} mg/mL, and all of the measurements were carried out above this concentration. Tetrabromocatechol (TBC) was purchased from Sigma-Aldrich. We prepared three TBC-loaded A27-B83 micelles with different loading ratios (w_{TBC} = 1.6, 2.4, and 4.0 wt %) as described in a previous article,[20] and w_{TBC} was determined from the UV absorbance of TBC (313 nm). We denote these samples PEAB-Br1.6, -Br2.4, and -Br4.0, respectively, and PEAB-0 the TBC-free A27-B83. With field flow fractionation coupled with multiangle light scattering with the incident wavelength of 658 nm (FFF-MALS),[21] the radius of gyration ($\langle S^2\rangle_{LS}^{1/2}$) and the weight-average molecular mass (M_w) for each polymeric micelle (note that M_w means the weight-average molar mass of the aggregated micelles including the probe molecules) were determined as described in our previous article.[14] From the chemical composition, the molar mass $M_{PEG\text{-}P[Asp(Bzl)]}$ of A27-B83 was determined as 1.03×10^4. Combining M_w and $M_{PEG\text{-}P[Asp(Bzl)]}$, the weight-average aggregation number $N_{agg,w}$ can be determined by $N_{agg,w} = (1 - w_{TBC}/100)\, M_w/M_{PEG\text{-}P[Asp(Bzl)]}$.

Synchrotron X-ray Scattering. All X-ray scattering measurements were performed at BL-40B2 of SPring-8, Japan with a 30 cm × 30 cm imaging plate (Rigaku R-AXIS VII). The measurements were conducted at five different energies E: 12.40 keV, noted as E_0, where the X-ray absorption of bromine is negligible, and 13.386, 13.436, 13.446, and 13.471 keV, which are near the absorption edge of bromine (13.486 keV). A bespoke SAXS vacuum sample chamber was used, and the X-ray transmittance of the samples was determined with an ion chamber located before the samples and a Si photodiode for X-rays (Hamamatsu Photonics S8193) after the samples.[15,22]

The micellar solutions were packed in a cell with a light path length of 3 mm and set in the sample chamber. SAXS from all sample solutions was measured for 45 s with the detector placed 1.65 m away from the sample. To obtain the excess scattering intensity of the micelles $I(q)$ at each q, which is the absolute value of the scattering vector $q = 4\pi \sin(\theta/2)/\lambda$, where θ is the scattering angle and λ is the incident wavelength, where E and λ can be related by λ (nm) = 12.4/E (keV), the background scattering of the buffer and the cell were subtracted after an appropriate transmittance correction. $I(q)$ was corrected to the absolute scale using the absolute scattering intensity of water of 1.632×10^{-2} cm^{-1}. The scattering experiments were carried out at concentrations of 1, 2, 3, and 40 mg/mL. Normal SAXS measurements were carried out for both dilute and concentrated solutions, while ASAXS measurements were only carried out for the concentrated solutions.

ASAXS analysis needs a larger signal-to-noise ratio than conventional SAXS. To achieve this, we used the vacuum sample chamber and exposed the sample for a longer time. To examine radiation damage of the samples, after collecting all data by changing the X-ray energy, we went back to the initial E and checked the reproducibility of the scattering profile. When the exposure time was shorter than 60 s for each measurement, there was no appreciable difference observed between the two profiles.

Data Analysis of Anomalous Small-Angle X-ray Scattering (ASAXS). When the scattering objects are presumed centro-symmetric and monodisperse, the SAXS intensity therefrom can be expressed by the product of the form factor P and the structure factor S.[23−25] This formulation can be extended to the case that the scattering length is changed with the incident X-ray energy on the same assumption (the

dx.doi.org/10.1021/ja308965j | J. Am. Chem. Soc. 2013, 135, 2574−2582

validity is discussed later). The energy-dependent scattering intensity $I(q)$ at a finite concentration of polymeric micelles can be expressed by

$$I(q, E, C_M) = \frac{M_w}{N_A} C_M[\rho_M(E) - \rho_0]^2 \bar{v}^2 P(q, E) S(q, C_M) \quad (1)$$

where N_A, C_M, $\rho_M(E)$, ρ_0, and $\bar{v}$ are the Avogadro number, the micellar mass concentration, the scattering lengths per volume of the micelle and solvent (cm^{-2}), respectively, and the specific volume of the micelle. The energy-dependent term is $(\rho_M(E) - \rho_0)^2\bar{v}^2P(q,E)$, and hereinafter, for convenience, we denote this term as $F(q, E)$. Because this contains all of the information for the spatial distribution of the probed atom, in this case Br, we needed to isolate it. To do so, we adopted the following procedure. At a particular energy E_0, far enough from the absorption edge to ignore the energy dependence of the intensity, the intensity at the infinite dilution, $I(q, E_0, 0)/c$ was obtained by $\lim_{c\to 0}[I(q, E_0, c)/c]$ at each q for the low concentrations. Here, for convenience, we use the mass concentration c instead of C_M. $I(q, E_0, 0)$ can be considered to contain only $F(q, E_0)$ as a q-dependent term. In our case, $S(q, c)$ is experimentally determined by the relation of $S(q, c) = [I(q, E_0, c)/c]/[I(q, E_0, 0)/c]$. This term is energy independent, and we can determine the F term for other energies as follows:

$$F(q, E) = \frac{I(q, E, C_M)}{KS(q, C_M)} \quad (2)$$

where $K = M_wC_M/N_A$. Scattering amplitude $A(q, E)$ can be expressed as $A(q, E) = F_0(q) + [f'(E) + if''(E)]v(q)$ by use of the real $f'(E)$ and imaginary $f''(E)$ parts of the resonant term, and the scattering amplitudes of the normal $F_0(q)$ and anomalous $v(q)$ components. Here, $v(q)$ is the scattering amplitude from the probe atoms. Note that $v(q)$ at $q = 0$ is proportional to only the number of the probe atoms, while $F_0(q)$ at $q = 0$ is proportional to the product of the number of all of the atoms and the averaged scattering length (details shown in the Supporting Information). $F(q, E)$ is the square of the absolute value of $A(q, E)$, tha tis, $|A(q, E)|^2 = A(q, E)A^*(q, E)$:

$$F(q, E) = F_0^2(q) + 2f'(E)F_0(q)v(q) + [f'^2(E) + f''^2(E)]v^2(q) \quad (3)$$

If the sample has no anomalous scattering, that is, $f'(E)$ and $f''(E)$ are approximated as 0, eq 3 is reduced to $F(q) = F_0^2(q)$. Regarding $F_0^2(q)$, $F_0(q)v(q)$, and $v^2(q)$ as three unknown functions, eq 3 is a linear equation with three unknowns. Therefore, to solve the equation, at least three different data sets with different X-ray energies are necessary, where $f'(E)$ and $f''(E)$ are given for each E.[18]

Fitting Models. Pedersen and Svaneborg's general scattering formula[26] for polymeric micelles can be simplified when the number of aggregated chains is large and the difference between the electron density of the shell chains and the solvent is relatively low as compared to the one between the core and the solvent. For a micelle with a specific size, the $I(q)$ can be expressed as follows:

$$\left(\frac{I(q, R_C)}{C_M}\right)_{C_M\to 0} = \frac{M_w}{N_A} \left\{(\rho_C - \rho_0)V_C \frac{3[\sin(qR_C) - qR_C\cos(qR_C)]}{(qR_C)^3} + 4\pi\int_{R_C}^{R_S}(\rho_S(r) - \rho_0)r^2 \sin(qr)/(qr)\, dr\right\}^2 \quad (4)$$

Here, R_C and R_S are the outer radii of the core and micelle, ρ_C, $\rho_S(r)$, and ρ_0 are the scattering lengths of the core, the shell, and the solvent, respectively, r is the distance from the center of the core, and N_A is the Avogadro number. A Daoud and Cotton type distribution was assumed for $\rho_S(r)$, where $\rho_S(r)$ decreases proportionally to $r^{-3/4}$, and at the inner limit of the shell, that is, $r = R_C$, $\rho_S(R_C) = \rho_{shell,in}$.[27,28]

To describe the distribution in the micellar size, we introduced a Gaussian function of $p(R_C)$ with a standard deviation of σ_{disp}, assuming that the deviation of the shell size (δR_S) is related to that of the core (δR_C) with $\delta R_S = (R_S/R_C)\delta R_C$:[28]

$$\left(\frac{I(q)}{C_M}\right)_{C_M\to 0} = \int_0^\infty p(R_C)\left(\frac{I(q, R_C)}{C_M}\right)_{C_M\to 0} dR_C \quad (5)$$

Because we used the absolute scattering intensities of water for intensity correction, the electron density (Ze: the number of electrons per unit volume, e/nm^3) for each layer can be obtained by $\rho/r_e = Ze$, where r_e is the classical radius of the electron: 2.818×10^{-13} cm. In eqs 4 and 5, M_w is obtained by LS in line with FFF and $\rho_0/r_e = 334\ cm^{-2}$. Thus, the remaining unknown parameters in eqs 4 and 5 are ρ_C, $\rho_{shell,in}$, R_C, R_S, and σ_{disp}. We determined these parameters with an iteration method described previously,[20] assuming that $\rho_0 = 334r_e < \rho_{PEG} < 369r_e$ and $R_C < R_S$, where ρ_{PEG} is the electron density of PEG in the solid state. The advantage of using M_w values obtained from the LS measurements and absolute intensities for $I(q)$ is that the range of acceptable values of the fitting parameters is reduced and the electron densities can be evaluated without ambiguity.

RESULTS

Determination of the Aggregation Number and the Size of the Micelles with Light Scattering. Figure 1 shows a typical FFF (field flow fractionation) fractogram of A27-B83/TBC micelles, where the smaller particles elute earlier (unlike size-exclusion chromatography) because the fractionation force is generated by a cross-flow field whose direction is perpendicular to the channel flow that elutes solutes through the channel.[29] The blue line corresponds to concentration detected by the differential refractive index (RI) detector, and the orange line corresponds to scattering intensity at the scattering angle of 90°. From the concentration and scattering intensity of each fraction, the molecular mass M and radius of gyration $\langle S^2\rangle^{1/2}$ were calculated. At 2−3 min on the RI chart a small peak was observed (indicated as A). This smaller component is most probably unreacted PEG or/and A27-B83 polymers that did not form micelles. The scattering intensity of this small peak was too small to calculate the molar mass and radius. The main peak at 6−9 min (B) corresponds to the A27-B83 polymeric micelles containing TBC. Here, the shapes of the main peak of RI and LS are similar to each other, which indicates narrow size distribution of our micelles. In fact, the polydispersity index of the micelles (shown in Table 1) is almost unity. The molar mass M_w, aggregation number $N_{agg,w}$, and radius of gyration $\langle S^2\rangle_{LS}^{1/2}$ are summarized in Table 1 for all samples. The refractive index increment dn/dc, number-average molar mass M_n, and polydispersity index M_w/M_n are also shown in Table 1. The M_w of PEAB-0, which was without TBC, is slightly larger than the other samples, but after the addition of TBC, M_w was almost the same for all samples within

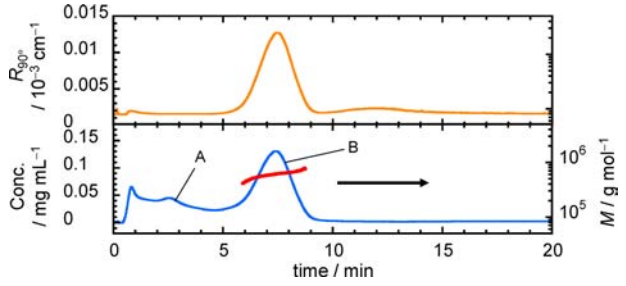

Figure 1. FFF fractogram of PEAB-Br2.4. The molar mass of each fraction of the peak is shown in red.

dx.doi.org/10.1021/ja308965j | J. Am. Chem. Soc. 2013, 135, 2574−2582

Table 1. Micellar Properties Determined by FFF-MALS

	w_{TBC}/wt %	dn/dc/cm^3 g^{-1}	$M_n \times 10^{-5}$/g mol^{-1}	$M_w \times 10^{-5}$/g mol^{-1}	$N_{agg,w}$	M_w/M_n	$\langle S^2\rangle_{LS}^{1/2}$/nm
PEAB-0	0	0.167	6.24	6.37	61.8	1.02	11.8
PEAB-Br1.6	1.6	0.169	5.68	5.76	55	1.03	8.9
PEAB-Br2.4	2.4	0.164	5.9	5.96	56.4	1.01	9.9
PEAB-Br4.0	4.0	0.166	5.86	5.9	54.9	1.01	9.8

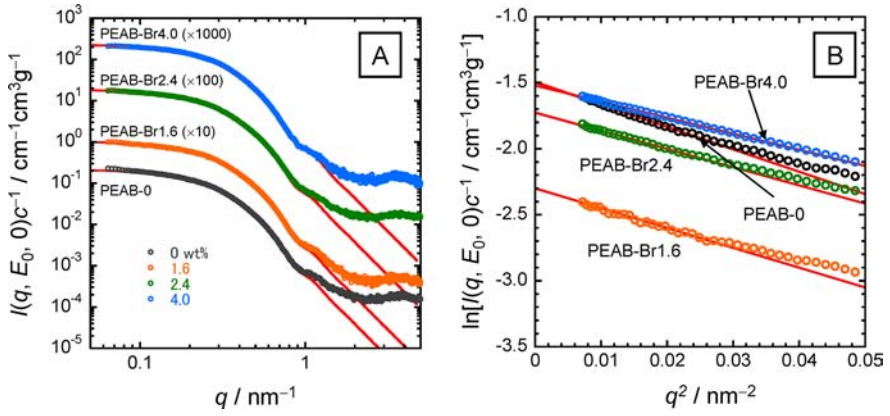

Figure 2. SAXS profiles obtained at the irradiation wavelength of 1 Å (12.4 keV), as compared to the theoretical values calculated from eq 4 (red lines) with the set of fitting parameters listed in Table 2 (A), and the Guinier plots ($\ln[I(q, E_0, 0)c^{-1}]$ vs q^2) of the small-angle region (B).

Table 2. Micellar Properties Determined by SAXS Measurements

	w_{TBC}/wt %	$\langle S^2\rangle_{SAXS}^{1/2}$/nm	R_C/nm	R_S/nm	$\rho_C r_e^{-1}/e$ nm^{-3}	$\rho_{shell,in} r_e^{-1}/e$ nm^{-3}	$\rho_0 r_e^{-1}/e$ nm^{-3}	σ_{disp}/R_C	σ_{PEG}
PEAB-0	0	7.1	4.5 ± 0.1	10.7 ± 0.4	407	338	334	0.22	2.5
PEAB-Br1.6	1.6	6.7	4.4 ± 0.1	10.3 ± 0.4	383	337	334	0.22	2.3
PEAB-Br2.4	2.4	6.4	4.5 ± 0.1	10.7 ± 0.4	403	337	334	0.22	2.3
PEAB-Br4.0	4.0	6.0	4.4 ± 0.1	9.8 ± 0.3	411	339	334	0.22	2.3

a range of ±5%. A similar pattern is observed for $\langle S^2\rangle_{LS}^{1/2}$; the value for PEAB-0 was larger than that for the other samples.

Structural Analysis of the Micelles with SAXS. Figure 2A compares the SAXS profiles $I(q, E_0, 0)/c$, the intensity extrapolated at the concentration of 0, for all samples at E_0 = 12.4 keV, where the X-ray energy is far below the Br absorption edge at 13.386 keV, and $I(q, E_0, 0)/c$ denotes the intensity at the infinite dilution limit. All samples showed the following features: q dependence of $I(q)$ was very small at $q < 0.1$ nm^{-1}, there were double-digit decreases at 0.2 nm$^{-1} < q < 1.0$ nm^{-1}, the second and high-q maxima were observed around q = 1.5 and 3.5 nm^{-1}, respectively, and between these two maxima, the intensities were almost constant at lower q region and the Porod power law, that is, $I(q) \approx q^{-4}$, could not be held at the higher q region. Because the profiles at $q < 1.0$ nm^{-1} showed a typical behavior of isolated scattering objects, we carried out the Guinier analysis as shown in Figure 2B. From the slope, we can calculate the radius of gyration $\langle S^2\rangle_{SAXS}^{1/2}$ from the relation of $\ln[I(q)] = \ln[I(0)] - 1/3\langle S^2\rangle_{SAXS} q^2$. We obtained $\langle S^2\rangle_{SAXS}^{1/2}$ for each sample, and the results are shown in Table 2. The presence of the second maximum indicated a rather narrow distribution of the micellar size. The intensity in the range of $q > 1.5$ nm^{-1}, including the high-q peak, reflects the atomic arrangement of the material and the density fluctuation. In our previous paper,[20] the high-q maximum in PEAB-0 was attributed to the ordering of the helices made from P[Asp(Bzl)] chains, called nonspecific hexatic arrangement. As shown in the paper, when LE540 (a highly hydrophobic retinoid antagonist drug; its chemical structure is shown in the Supporting Information) was loaded, the peak intensity became drastically weaker with increasing LE540 and eventually disappears. For the present case, the high-q peak was not eliminated. We discuss this issue later.

By use of eq 5, the experimental data were well fitted to the theoretical curves (Figure 2A, solid line) in the range of $q < 1.0$ nm^{-1}. By contrast, in the high-q range ($q > 1.0$ nm^{-1}), the experimental values were deviated upward from the theoretical lines. This can be ascribed to the atomic scale density fluctuation of the core-constituting chains (i.e., the edge of amorphous halo) or/and the shell-chain conformational fluctuation. The agreement can be improved by adding a Debye function[26] to describe the shell-chains and an empirical equation to describe the amorphous halo,[30] but these corrections did not alter the obtained structural parameters.

The obtained parameters R_C, R_S, ρ_C, $\rho_{shell,in}$, ρ_0, and σ_{disp} are shown in Table 2. The values of the radius of the core R_C and the whole micelle R_S are almost the same for all samples with R_C having a relative small error while R_S has a relative large error. It should be noted that the electron densities of the core and inner limit of the shell were determined with no assumptions thanks to the M_w values determined from FFF-MALS. The values of σ_{disp}/R_C were almost the same for all samples, suggesting that the addition of TBC did not affect the size dispersity of the micelles. Comparing σ_{disp}/R_C with M_w/M_n in Table 1, we can conclude that the micellar shapes showed some amount of dispersity, while the molar mass was close to monodisperse.

Structure Factor Correction. Figure 3A shows $I(q, E_0, 0)/c$ and $I(q, E_0, 40)/c$ as red and black dots, respectively. The black circles deviate from the red ones upward around q = 0.25

dx.doi.org/10.1021/ja308965j | J. Am. Chem. Soc. 2013, 135, 2574−2582

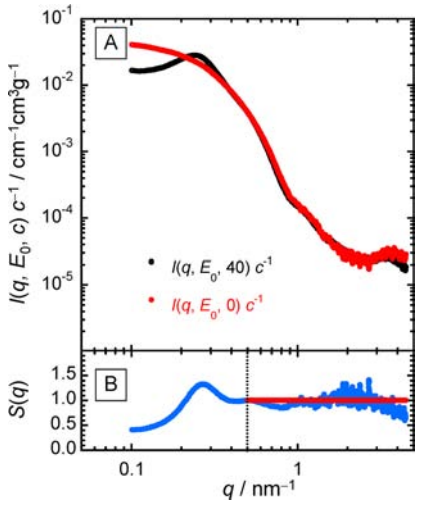

Figure 3. SAXS profiles of PEAB-Br2.4 at 40 mg/mL and at (extrapolated) zero concentration (A). Calculated structure factor of PEAB-Br2.4 (B). Blue dots show the division of the profile at 40 mg/mL with the one at zero concentration. The structure factor where $S(q) = 1$ at $q > 0.5$ is shown as red circles.

nm^{-1} and downward at $q < 0.20$ nm^{-1}. This is a typical feature of scattering profiles where the interparticle interference factor cannot be ignored.[30] As presented in the Supporting Information (Figure S2), because the extrapolation to the infinite dilution was successfully carried out, we can consider that $S(q, 0) = 1$ in $I(q, E_0, 0)/c$. Therefore, the structure factor at $c = 40$ mg/mL can be obtained by dividing $I(q, E_0, 40)/c$ with $I(q, E_0, 0)/c$. Figure 3B shows the structure factor thus obtained against q; at $q < 0.5$ nm^{-1}, it showed the anticipated behavior, while at $q \geq 0.5$ nm^{-1}, where the structure factor is expected to converge to 1, it did not. This deviation is due to the low signal-to-noise ratio when the intensity is low. For further calculations, we presume $S(q, 40) = 1$ at $q > 0.5$ nm^{-1} as shown in Figure 3B with the red line.

As mentioned in the Experimental Section, to apply eq 1 to our system, it is necessary to assume that A27-B83/TBC micelle is monodisperse and centro-symmetric. Strictly speaking, this assumption is not true because σ_{disp}/R_C in Table 2 was 0.22. Therefore, $S(q\ C_M)$ in eq 1 is regarded as the effective structural factor $S_{eff}(q\ C_M)$, which can be related to the real E-independent structural factor, $S(q,C_M)$, with the following equation:[25]

$$S_{eff}(q, E, C_M) = 1 + \beta(q, E)[S(q, C_M) - 1] \quad (6)$$

Here, β is a q and E-dependent factor changing between zero and one and defined as the ratio of $|\langle A(q,E)\rangle|^2/\langle|A(q,E)|^2\rangle$. For the present case, the weight percent of Br atoms was at most 0.74%, meaning that the difference of β at $E_{Br} = 13.486$ keV (absorption edge of Br, $f' = -7.374$) and $E_0 = 12.40$ keV ($f' \approx 0$) is less than 1% (see Supporting Information Figure S3). This leads that $S_{eff}(q, C_M)$ is essentially independent of E for the present case. As mentioned, we obtained $S_{eff}(q, C_M)$ at E_0 and determined $F(q, E)$ for different E for the exactly same C_M; therefore, we can consider that thus obtained $F(q, E)$ is valid. Pedersen discussed the case that polymeric micelles are not strictly centro-symmetric.[31] According to his paper, the effective structural factor can be expressed by an equation similar to eq 6. Therefore, as far as very small contrast difference between different energies, our procedure should give an accurate form factor at each energy.

The structure factor is directly related to the correlation function between the scattering particles.[25,30,31] We tried to fit the obtained effective structure factor (Figure 3B) with the hard-sphere model (see Figure S4).[32] When we considered the distribution of the micellar shape (i.e., eq 6), there was some improvement, but either model cold not fit the data satisfactory.

Determination of the Resonant Term and Distribution of Br. Figure 4A and B shows $I(q, E, 40)/c$ and $I(q, E, 40)/[cS(q, 0)]$, respectively, for five different X-ray energies at $c = 40$ mg/mL. As shown in the inset, while approaching the Br absorption edge (13.486 keV), the intensities decreased around $q = 0.1$ and 0.4 nm^{-1}, due to the decrease in the scattering length of Br. We solved the system of three linear equations with three unknowns given based on eq 3 to obtain the resonant term. Figure 5 shows the resonant term $\nu^2(q)/c$ (blue ○) juxtaposed to $I(q, E_0, 0)/c$ (○) for PEAB-Br1.6, -Br2.4, and -Br4.0. The intensity difference between the two terms is over 1 order of magnitude for all q, as expected.

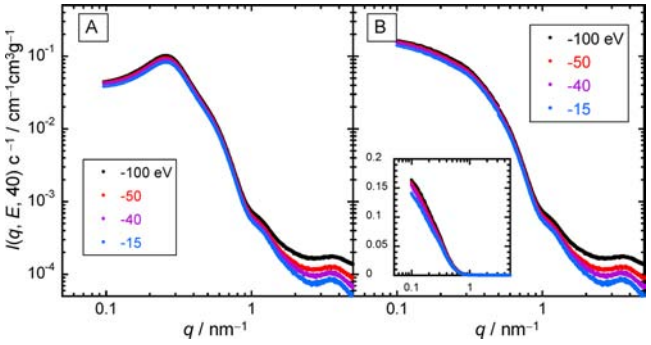

Figure 4. SAXS profiles of PEAB-Br2.4 at 40 mg/mL concentration obtained at several X-ray energies (A), and the same profiles after correction with the structure factor shown in Figure 3 (B). The legend shows the energy difference with the absorption edge.

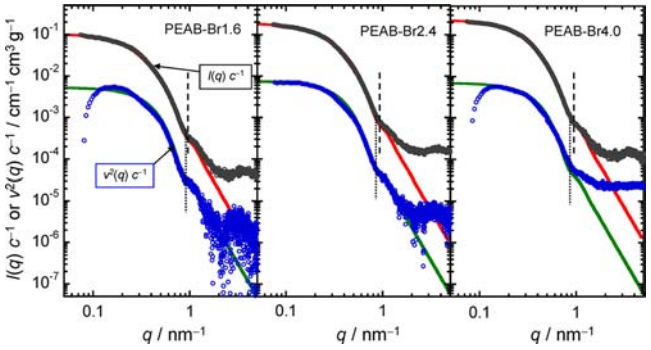

Figure 5. SAXS profiles (○), resonant terms of the polymeric micelles (blue ○), and theoretical curves calculated from hard-sphere models with dispersity (red lines for SAXS profiles, green lines for resonant terms).

The q dependence of $\nu^2(q)$ is consistent with that of spherical objects, as expected because TBC molecules are considered to distribute all over the spherical core. Although the intensities were low and with a lower S/N ratio than $I(q, E_0, 0)/c$, we can still observe an inflection point in all $\nu^2(q)$ plots exhibited between the first and second maxima, the position of which is indicated with dotted lines. In common with Figure 2, the

dx.doi.org/10.1021/ja308965j | J. Am. Chem. Soc. 2013, 135, 2574−2582

presence of the inflection point indicated narrow distribution in size and is related to the size of the scattering objects. In the case of a hard-sphere with a radius R, for example, the relation of $R \times q^* = 4.493$ can be applied, where q^* is the position of the inflection point. The inflection points are also indicated with dashed lines for $I(q, E_0, 0)/c$ in the figure. The positions of the dotted lines are independent of the TBC loading ratio, which is consistent with the fact that their R_C and N_{agg} are not affected by the loading ratio. In contrast, the position of the inflection point in $\nu(q)^2$ shifted toward the low q side upon loading, indicating that the size of the TBC-containing region became enlarged with incremental addition of TBC. By assuming that its shape is a hard-sphere, $\nu(q)^2$ was fitted and the obtained radii R_{Br} as well as the standard deviations σ_{Br}/R_{Br} are summarized in Table 3. When the TBC loading increased from 1.6 to 4.0 wt %, R_{Br} increased from 4.6 ± 0.1 to 4.8 ± 0.2 nm. As compared to the radii of the core of the respective micelles, the increment was only 0.2−0.4 nm; however, this value is larger than the experimental error and thus statistically significant.

Table 3. Hard-Sphere Model Parameters of the Bromine Region Determined from ASAXS Analysis

	w_{TBC}/wt %	R_{Br}/nm	σ_{Br}/R_{Br}
PEAB-Br1.6	1.6	4.6 ± 0.1	0.22
PEAB-Br2.4	2.4	4.8 ± 0.1	0.22
PEAB-Br4.0	4.0	4.7 ± 0.2	0.22

As described in the Experimental Section, $\nu(q)$ represents the scattering amplitude of the Br atoms, and the value of $\nu(q = 0)$ is directly related to the number of the Br atoms. In Figure 5, the value of $\nu^2(q)/c$ extrapolated to $q \to 0$ increased as the TBC loading ratio increased. This result was consistent with increasing Br atoms. The magnitude of the background at $q > 2$ nm^{-1} also increased as the TBC loading ratio increased. Because the background is due to atomic scale ordering and its thermal fluctuation[30] and those of the resonant term should be only ascribed to Br, the increasing background is also related to the increase of the number of Br atoms.

DISCUSSION

Analysis of ASAXS Data. To obtain $\nu^2(q)$, we solved a system of three equations based on eq 3. Although this is rather straightforward, there is no way to take into account experimental errors. Dingenouts et al.[18] proposed another method; they measured $I(q, E)$ at several E and constructed the interpolated relation of $I(q, E)$ versus $f'(E)$ and obtained $F_0(q)$ and $\nu^2(q)$ from eq 3. An advantage of their method is that it reduces experimental errors creeping into the determination of $f'(E)$. By following their procedure, we determined $\nu^2(q)$. Because there was not much difference between the profiles obtained from the two methods (see Figures S5, S6), we chose the profile obtained from eq 3.

Figure 5 shows that $\nu^2(q)/c$ deviates slightly from the theoretical curves, but an especially appreciable downward deviation was observed for all three different TBC loading ratios around $q = 0.4$ nm^{-1}. This q range coincides with the second minimum of the structure factor $S(q, 40)$. This coincidence suggested that the elimination of the structure factor from the observed scattering may not be complete enough. When the polymer concentration is decreased, the structure factor becomes less significant because it asymptotically approaches 1. Therefore, one might argue that it would have been better to measure solutions more dilute than $c = 40$ mg/mL. However, such dilute conditions do not provide intensities large enough to extract the resonant term. After taking into account the trade-off between the magnitude of the intensity and the significance of the structure factor, we decided that the S/N ratio was more important to our analysis.

Core Size Change upon Drug-Loading. Akiba et al.[20] examined how the overall micellar architecture was changed upon loading the highly hydrophobic compound LE540 (the chemical structure is shown in Figure S1 in the Supporting Information), an artificial hydrophobic retinoid. With increasing loading ratio, the core size and the aggregation number increased. This behavior means that the addition of more hydrophobic molecules into the core increases its hydrophobicity, leading to an increase in the aggregation number. On the contrary, when adding TBC, such increase was not observed. As presented in Tables 1 and 2, the core size R_C and the radius of gyration $\langle S^2 \rangle^{1/2}$ stayed almost the same or slightly decreased upon loading TBC. We presume that this is related to the fact that TBC is less hydrophobic than LE540. We observed the same phenomenon when adding Am80 (chemical structure shown in the Supporting Information), which is also less hydrophobic than LE540.

As mentioned in the Results, Akiba et al. found that the third peak intensity became drastically weaker with increasing LE540 and eventually disappears. The decrease in the peak intensity corresponds to a decrease in the ordering of the P[Asp(Bzl)] helices. This phenomenon can be interpreted as a uniform distribution of LE540 in the P[Asp(Bzl)] core, and the interaction between LE540 and P[Asp(Bzl)] is more favorable than the helix formation of P[Asp(Bzl)]. In the case of TBC loading, we did not observe such disappearance of the peak, although the peak became less pronounced with increasing TBC concentration. Am80 showed behavior similar to that of TBC (see Supporting Information Figure S7). This difference between LE540 and TBC also can be explained by the difference in hydrophobicity between them.

Overcrowding Nature of PEG. At the interface between the spherical core and the shell region, the surface density of the PEG chains can be discussed in terms of the following parameter:[33]

$$\sigma_{PEG} = \frac{N_{agg}\pi\langle S^2\rangle_{PEG}}{4\pi(R_C + \langle S^2\rangle_{PEG}^{1/2})^2} \quad (7)$$

where $\langle S^2\rangle_{PEG}^{1/2}$ is the radius of gyration of the PEG single chain; in our case, $M_w = 5200$, $\langle S^2\rangle_{PEG}^{1/2} = 3$ nm. The value of σ_{PEG} represents the ratio of the surface area covered with PEG shell chains. When $\sigma_{PEG} < 1$, the interface of the core is not overspread with shell chains and the chains are isolated from each other.[34] If $\sigma_{PEG} = 1$, the interface of the core is just covered with shell chains completely, and with further increase of σ_{PEG} the chains in the shell region become crowded and finally they become more stretched. The σ_{PEG} values for our four samples are shown in Table 2. All samples have almost the same value of $\sigma_{PEG} \approx 2.3$, which indicates that the shell region of the micelles is completely covered with PEG chains but not crowded enough to cause significant stretching. This magnitude of σ_{PEG} suggests that tethering of the PEG chains causes some amount of water to be excluded from the shell, an amount that would immerse and solubilize the PEG chain if that same PEG chain was free in solution. This means that the PEG chains

dx.doi.org/10.1021/ja308965j | J. Am. Chem. Soc. 2013, 135, 2574−2582

environment becomes slightly less hydrophilic, and this change would be more pronounced in the vicinity of the core/shell interface.

Confirming That the Br Sphere Is Larger than the Core. The green lines in Figure 5 show the theoretical intensities calculated from hard-sphere models with sphere radii of 4.6, 4.8, and 5.0 nm for PEAB-Br1.6, -Br2.4, and -Br4.0, respectively. The theoretical curves were in good agreement with the experimental results. These radii are all larger than the radii of the cores of the micelles shown in Table 2 and Figure 6.

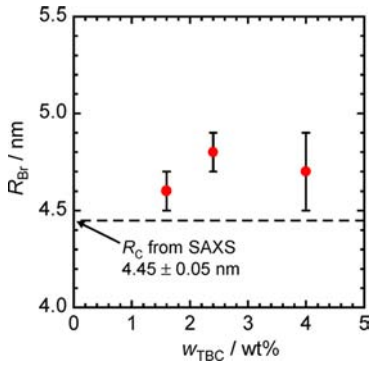

Figure 6. Plot of the radius of the bromine sphere (R_{Br}) versus TBC loading ratio. The dashed line represents the averaged micellar core radius (R_C) without TBC, determined with SAXS.

Again, the fact that the Br-containing sphere is larger than the core is consistent with the shift of the second minimum position. This result is consistent with the difference in the slope of the Guinier plots constructed from $v^2(q)$ and $I(q, E_0, 0)/c$, although the incomplete correction for the structure factor makes the plots rather noisy (see Supporting Information Figure S8).

Before reaching a conclusion, it is better to consider the possibility that the Br distribution is confined within the core, but gives a lager radius of gyration than that expected from the hard-sphere. This can happen when Br atoms are distributed more densely at the edge of the core than at its center. To simulate such a situation, we assumed a model where the electron density increases with the distance from the center of the core along a Gaussian distribution, and the highest density is set at the outer limit of the region. The electron density of the Br-containing region was calculated using the following formulas:

$$v_{theor}{}^2(q) = \int_0^\infty p(R_{Br}) \cdot n\left\{4\pi \int_0^{R_{Br}} \rho_{Br}(r) r^2 \sin(qr)/(qr)\, dr\right\}^2 dR_{Br} \quad (8)$$

$$\rho_{Br}(r) = \begin{cases} \rho_{Br,inner} + (\rho_{Br,outer} - \rho_{Br,inner}) & r \le R_{Br} \\ \dfrac{1}{\sqrt{2\pi\sigma_{Br}{}^2}} \times \exp\left(-\dfrac{(R_{Br}-r)^2}{2\sigma_{Br}{}^2}\right) & \\ 0 & r > R_{Br} \end{cases} \quad (9)$$

where R_{Br} is the outer limit of the bromine region (=R_C, in this case), $\rho_{Br,inner}$ and $\rho_{Br,outer}$ are the inner and the outer limits of the atom densities of the bromine atoms, and σ_{Br} is the variance of the distribution of the bromine. When $\rho_{Br,inner} = \rho_{Br,outer}$, the formula is reduced to that of the hard-sphere model. Here, we fixed the number of the electron, that is, number of Br atoms, so as to give the same values for $v_{theor}{}^2(q)/c$ extrapolated at $q \to 0$ (Figure 7A).

The blue and green lines in Figure 7 show the theoretical curves for the models described above. These two lines cannot explain the experimental data satisfactorily. The red line shows the theoretical curve of the hard-sphere model with optimized radius, and it is better fitted to the experimental data than the other two. The calculated residual errors are shown in the inset of Figure 7, confirming that the hard-sphere model is better than the others. Around q = 0.2, all three theoretical curves have small residual errors less than 20%, but with increasing q values, the errors of the blue and green lines increased about 50%. Despite that, the error of the red line remained low. The parameters for the red line are shown in Table 3. With the above results, it is reasonable to conclude that the bromine-containing region is larger than the core of the micelle, which means that some amount of TBC infiltrates into the core−PEG interface.

Molecular Interpretation of the Bigger Br Sphere. As described above, the bromine-containing region is larger than

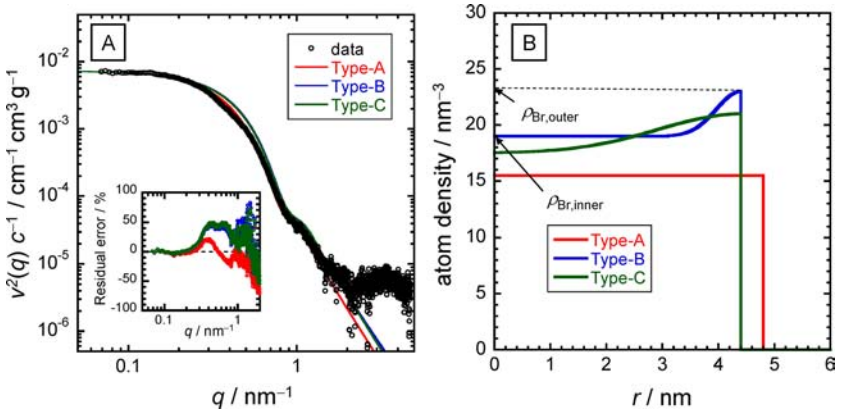

Figure 7. Resonant term of PEAB-Br2.4 and theoretical curves of the model described by eq 8 against q (A). Atom density versus distance r from the center of the particle (B). The parameters for the theoretical curves were as follows: Type-A, $\rho_{Br,inner} = \rho_{Br,outer}$ = 15.5; Type-B, $\rho_{Br,inner}$ = 17.5, $\rho_{Br,outer}$ = 21.0, σ_{Br} = 1.46; Type-C, $\rho_{Br,inner}$ = 17.5, $\rho_{Br,outer}$ = 21.0, σ_{Br} = 0.43.

dx.doi.org/10.1021/ja308965j | J. Am. Chem. Soc. 2013, 135, 2574−2582

the micelle core. This result indicates that a hydrophobic compound can exist not only at the core but also outside the core (in our case in an area 0.5 nm thick). Figure 6 shows the radius (of a hard-sphere model) of the bromine-containing region R_{Br} versus w_{TBC}. R_{Br} increases with increasing values of w_{TBC}. From previous experiments (data not shown), we know that the maximum amount of TBC that the polymeric micelle can contain is about 4 wt %. Above that value, TBC starts to precipitate. These observations lead to the following explanation. At first, when the amount of TBC is less than about 1 wt %, TBC disperses only in the hydrophobic core. However, increasing the amount of TBC to about 1.5−4.0 wt % causes TBC to start spreading out of the core. Finally, amounts greater than 4.0 wt % are beyond the capacity of the polymeric micelle.

TBC exists in the shell region where PEG chains come in contact with the aqueous medium. Of course, PEG is known as a "water-soluble" material, but the chemical structure of PEG can be also hydrophobic like all ethers. As shown from the analysis of the core−corona model, the concentration of PEG chains decreases with increasing distance from the center of the core, because one end of the PEG chain is tethered to the interface of the core, and as one moves away from the core the surface area increases while the number of chains remains the same. The interface to the core has the highest concentration of PEG chains, which would make it the most hydrophobic part of the shell region rendering TBC "soluble" to the PEG region (Figure 8).

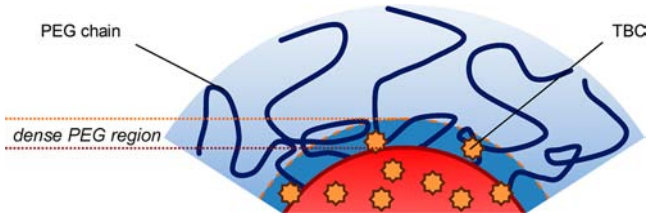

Figure 8. Schematic representation of the TBC distribution in the micelle. The red region represents the hydrophobic core, blue lines represent PEG chains, and orange polygons represent TBC.

CONCLUSION

From SAXS and LS measurements, the sizes and aggregation numbers of the micelles containing various amounts of the hydrophobic compound TBC were determined. The sizes and aggregation numbers of the micelles were not essentially affected by changing the loading ratio of TBC. On the other hand, the resonant term of bromine calculated from ASAXS measurements showed the dispersion behavior of the TBC in the hydrophobic core. The result indicates that excess amount of TBC causes it to spread out of the core, and we believe that these TBC molecules exist at the interface between the core and the shell region where PEG chains are highly dense. It is not easy to obtain detailed information about the distribution of compounds in the hydrophobic core of a micelle from traditional methods such as DLS or microscopy. The insight obtained on the inner structure of the micelles or other DDS loaded with medical agents can contribute to the construction of novel DDS systems.

ASSOCIATED CONTENT

Supporting Information

Details of synthesis of the copolymer, scattering amplitude of ASAXS analysis, supplementary chemical structures, SAXS profiles with concentration dependence, calculated $\beta(q, E)$ for the core−corona model, comparison of $S(q)$ from the experiments and the theoretical model, X-ray energy dependence of $I(q, E, c)$, resonant terms calculated from Dingenouts' method, SAXS profiles of the Am80 loaded micelles, and Guinier plot of the resonant terms. This material is available free of charge via the Internet at http://pubs.acs.org.

AUTHOR INFORMATION

Corresponding Author

sakurai@kitakyu-u.ac.jp

Notes

The authors declare no competing financial interest.

ACKNOWLEDGMENTS

This work was financially supported by a JST CREST program, and all SAXS measurements were carried out at the SPring-8 beamline 40B2 (2010B1726, 2011A1668, 2011B1735).

REFERENCES

(1) Yu, Y.; Eisenberg, A. *J. Am. Chem. Soc.* **1997**, *119*, 8383−8384.
(2) Hamley, I. W. *The Physics of Block Copolymers*; Oxford University Press: Oxford, 1998; Chapter 3: Block copolymers in dilute solution, pp 131−220.
(3) Harada, A.; Kataoka, K. *Macromolecules* **1998**, *31*, 288−294.
(4) Matsumura, Y.; Kataoka, K. *Cancer Sci.* **2009**, *100*, 572−579.
(5) Kataoka, K.; Harada, A.; Nagasaki, Y. *Adv. Drug Delivery Rev.* **2001**, *47*, 113−31.
(6) Yang, Y. Q.; Zheng, L. S.; Guo, X. D.; Qian, Y.; Zhang, L. J. *Biomacromolecules* **2010**, *12*, 116−122.
(7) Waku, T.; Matsusaki, M.; Kaneko, T.; Akashi, M. *Macromolecules* **2007**, *40*, 6385−6392.
(8) Hadjichristidis, N.; Iatrou, H.; Pitsikalis, M.; Sakellariou, G. *Chem. Rev.* **2009**, *109*, 5528−5578.
(9) Yokoyama, M.; Opanasopit, P.; Okano, T.; Kawano, K.; Maitani, Y. *J. Drug Targeting* **2004**, *12*, 373−384.
(10) Yokoyama, M.; Okano, T.; Sakurai, Y.; Ekimoto, H.; Shibazaki, C.; Kataoka, K. *Cancer Res.* **1991**, *51*, 3229−3236.
(11) Bae, Y.; Nishiyama, N.; Fukushima, S.; Koyama, H.; Yasuhiro, M.; Kataoka, K. *Bioconjugate Chem.* **2004**, *16*, 122−130.
(12) Adams, M. L.; Andes, D. R.; Kwon, G. S. *Biomacromolecules* **2003**, *4*, 750−757.
(13) Yamamoto, T.; Yokoyama, M.; Opanasopit, P.; Hayama, A.; Kawano, K.; Maitani, Y. *J. Controlled Release* **2007**, *123*, 11−8.
(14) Sanada, Y.; Akiba, I.; Hashida, S.; Sakurai, K.; Shiraishi, K.; Yokoyama, M.; Yagi, N.; Shinohara, Y.; Amemiya, Y. *J. Phys. Chem. B* **2012**, *116*, 8241−8250.
(15) Naruse, K.; Eguchi, K.; Akiba, I.; Sakurai, K.; Masunaga, H.; Ogawa, H.; Fossey, J. S. *J. Phys. Chem. B* **2009**, *113*, 10222−10229.
(16) Cromer, D. T.; Liberman, D. *J. Chem. Phys.* **1970**, *53*, 1891−1898.
(17) Stuhrmann, H. Resonance scattering in macromolecular structure research. Characterization of Polymers in the Solid State II: Synchrotron Radiation. In *X-ray Scattering and Electron Microscopy*; Kausch, H., Zachmann, H., Eds.; Springer: Berlin/Heidelberg, 1985; Vol. *67*, pp 123−163.
(18) Dingenouts, N.; Patel, M.; Rosenfeldt, S.; Pontoni, D.; Narayanan, T.; Ballauff, M. *Macromolecules* **2004**, *37*, 8152−8159.
(19) Kabanov, A. V.; Batrakova, E. V.; Alakhov, V. Y. *J. Controlled Release* **2002**, *82*, 189−212.

(20) Akiba, I.; Terada, N.; Hashida, S.; Sakurai, K.; Sato, T.; Shiraishi, K.; Yokoyama, M.; Masunaga, H.; Ogawa, H.; Ito, K.; Yagi, N. *Langmuir* **2010**, *26*, 7544−7551.
(21) Guyomarc'h, F.; Violleau, F. d. r.; Surel, O.; Famelart, M.-H. l. n. *J. Agric. Food Chem.* **2010**, *58*, 12592−12601.
(22) Akiba, I.; Takechi, A.; Sakou, M.; Handa, M.; Shinohara, Y.; Amemiya, Y.; Yagi, N.; Sakurai, K. *Macromolecules* **2012**, *45*, 6150−6157.
(23) Mortensen, K.; Pedersen, J. S. *Macromolecules* **1993**, *26*, 805−812.
(24) Sztucki, M.; Di Cola, E.; Narayanan, T. *J. Appl. Crystallogr.* **2010**, *43*, 1479−1487.
(25) Kotlarchyk, M.; Chen, S.-H. *J. Chem. Phys.* **1983**, *79*, 2461−2469.
(26) Pedersen, J. S.; Svaneborg, C.; Almdal, K.; Hamley, I. W.; Young, R. N. *Macromolecules* **2003**, *36*, 416−433.
(27) Daoud, D.; Cotton, J. P. *J. Phys.* **1982**, *43*, 531−538.
(28) Nakano, M.; Deguchi, M.; Matsumoto, K.; Matsuoka, H.; Yamaoka, H. *Macromolecules* **1999**, *32*, 7437−7443.
(29) Hoppe, C.; Nguyen, L.; Kirsch, L.; Wiencek, J. *J. Biol. Eng.* **2008**, *2*, 10.
(30) Roe, R. J. *Methods of X-ray and Neutron Scattering in Polymer Science*; Oxford University Press: Oxford, 2000.
(31) Pedersen, J. S. *J. Chem. Phys.* **2001**, *114*, 2839−2846.
(32) Ashcroft, N. W.; Lekner, J. *Phys. Rev.* **1966**, *145*, 83−90.
(33) Svaneborg, C.; Pedersen, J. S. *Macromolecules* **2002**, *35*, 1028−1037.
(34) Chen, W. Y.; Zheng, J. X.; Cheng, S. Z. D.; Li, C. Y.; Huang, P.; Zhu, L.; Xiong, H.; Ge, Q.; Guo, Y.; Quirk, R. P.; Lotz, B.; Deng, L.; Wu, C.; Thomas, E. L. *Phys. Rev. Lett.* **2004**, *93*, 028301.